



Subtomogram analysis using the Volta phase plate



Maryam Khoshouei^{a,1}, Stefan Pfeffer^{a,1}, Wolfgang Baumeister^a, Friedrich Förster^{a,b,*}, Radostin Danev^{a,*}

^a Max-Planck Institute of Biochemistry, Department of Molecular Structural Biology, Am Klopferspitz 18, 82152 Martinsried, Germany

^b Cryo-Electron Microscopy, Bijvoet Center for Biomolecular Research, Utrecht University, Padualaan 8, 3584 CH Utrecht, The Netherlands

ARTICLE INFO

Article history:

Received 17 March 2016

Received in revised form 6 May 2016

Accepted 24 May 2016

Available online 25 May 2016

Keywords:

Cryo-electron tomography

Subtomogram analysis

Volta phase plate

Ribosome

ABSTRACT

Cryo-electron tomography (CET) and subtomogram analysis allow studying the structures of macromolecular complexes in their natural context. The radiation sensitivity of vitrified biological specimens and the resulting low signal-to-noise ratio (SNR) in CET limit the amount of structural information that can be mined from tomographic data. The Volta phase plate (VPP) has emerged as an effective means to increase the SNR and hence contrast compared to 'conventional' defocus-based phase contrast transmission electron microscopy (CTEM). Here, we assess the performance of the VPP compared to CTEM in subtomogram analysis, using the mammalian 80S ribosome as a test case. Accurate focusing is the major factor for achieving high resolution with the VPP, as highlighted by a comparison of slightly different focusing strategies. From only 1400 subtomograms, the VPP yields a subtomogram average of the mammalian 80S ribosome at 9.6 Å resolution without laborious contrast transfer function (CTF) correction. The subtomogram averages obtained using CTEM approaches are comparable, but suffer from lower signal transfer in certain frequency bands due to the oscillations of the CTF. Our study demonstrates that the VPP is a valuable tool for subtomogram analysis, because it enables improved performance and efficiency in terms of structure localization and number of subtomograms required for a given resolution.

© 2016 Elsevier Inc. All rights reserved.

1. Introduction

Cryo-electron tomography (CET) can provide three-dimensional (3D) views of structures and molecular organizations in a wide range of cryo-preserved specimens under near-to-native conditions (Lucic et al., 2013). It is applicable to a variety of cell-free systems, isolated cellular organelles and even intact cells. In combination with advanced image processing methods ('subtomogram analysis'), the location, orientation and, in particular, the structure of larger macromolecular complexes can be extracted from tomographic data (Briggs, 2013; Förster and Hegerl, 2007). CET is an excellent method for studying the molecular machine responsible for cellular protein synthesis, the ribosome, in a native context (Brandt et al., 2009; Myasnikov et al., 2014; Pfeffer et al., 2015; Pfeffer et al., 2012; Pfeffer et al., 2014). The ribosome is a universally conserved RNA-protein complex of 3–4 MDa size consisting of two subunits, which in concert

mediate decoding of messenger RNA and formation of peptide bonds in the growing polypeptide chain (Steitz, 2008). Due to its fundamental importance, the ribosome has been extensively studied using single particle cryo-electron microscopy (cryo-EM) (Anger et al., 2013; Behrmann et al., 2015; Voorhees et al., 2014) and X-ray crystallography (Ben-Shem et al., 2010; Ben-Shem et al., 2011; Jenner et al., 2012; Schuwirth et al., 2005; Selmer et al., 2006; Yusupov et al., 2001), yielding structural insights into protein synthesis with atomic detail.

The low signal-to-noise ratio (SNR) of CET data limits their molecular interpretability in two ways: (i) CET is mostly used to image native or close-to-native samples, which contain numerous different types of macromolecular complexes. In-depth analysis of a macromolecule of interest requires its specific and sensitive detection, for example by template matching (Förster et al., 2010; Frangakis et al., 2002). The SNR is a key determinant for the specificity and sensitivity of the localization of macromolecules. (ii) Subtomogram averaging allows *in silico* enhancement of the signal and hence increases the resolution compared to that of raw tomograms. The attainable resolution depends not only on the number of averaged subtomograms, but also on their SNR, which determines how accurately they can be aligned to a common reference.

* Corresponding authors at: Max-Planck Institute of Biochemistry, Department of Molecular Structural Biology, Am Klopferspitz 18, 82152 Martinsried, Germany.

E-mail addresses: foerster@biochem.mpg.de (F. Förster), danev@biochem.mpg.de (R. Danev).

¹ These authors contributed equally.

Both the detection fidelity and the accuracy of subtomogram alignment depend primarily on the low-frequency components of the signal, which are by far the strongest for any macromolecular complex (Scheres and Chen, 2012). Defocus-based phase contrast severely dampens the low-frequency components and has contrast transfer function (CTF)-induced contrast oscillations at higher frequencies, which necessitate elaborate correction methods for faithful interpretation of the data. These contrast oscillations also result in the absence of signal for spatial frequencies located close to the CTF zeros. In comparison, a phase plate (PP) introduces a relative phase shift between the scattered and unscattered electrons, which allows imaging in or close-to focus with strong and continuous contrast transfer from low to high frequencies. The increase of low frequency contrast, in particular, promises to be highly beneficial for CET because particles can be localized and aligned more accurately.

The recently introduced Volta PP (VPP) is the first implementation of a PP for electron microscopy that is sufficiently durable and easy to use for routine work (Danev et al., 2014; Fukuda et al., 2015). The VPP consists of a thin amorphous carbon film mounted on a supporting aperture positioned at the back-focal plane of the objective lens of the microscope. The Volta potential created by the electron beam on the surface of the heated amorphous carbon film induces a phase shift for the unscattered electron beam, which leads to a change in the contrast transfer function and improved contrast (Danev et al., 2014). After initial conditioning of the VPP, the phase shift remains approximately constant and changes only very gradually. Tomographic data acquisition with the VPP requires accurate focusing in order to provide uniform, oscillation-free information transfer throughout the frequency spectrum. The position of the sample changes during sequential tilting of the specimen, requiring accurate measurement and adjustment of the microscope defocus for each tilt image. Perpendicular to the tilt-axis tilt images exhibit a defocus gradient, which complicates data acquisition further. The VPP has already proven its value for CET (Asano et al., 2015; Fukuda et al., 2015; Mahamid et al., 2016) and cryo-EM single particle analysis (Danev and Baumeister, 2016; Khoshouei et al., 2016) but its performance in subtomogram analysis has not yet been quantitatively evaluated.

Here, we assess the performance of the VPP for subtomogram analysis and compare it to CTM. In particular, we investigate whether subtomogram averages of subnanometer resolution can be obtained using the VPP and what is the best strategy for data acquisition. We chose the mammalian 80S ribosome as a test sample because it is highly abundant, structurally well characterized and, due to its size, suitable for subtomogram analysis.

2. Materials and methods

2.1. Sample preparation and CET

Ribosomes were pelleted (TLA 100, 30 min, 150,000 g, 4 °C) from rabbit reticulocyte lysate (Promega, USA) and resuspended in ribosome buffer (20 mM Hepes, pH 7.6; 50 mM KCl; 2 mM MgCl₂). After applying 3 µl of ribosomes to plasma-cleaned (20 s) Quantifoil R 2/1 (Quantifoil, Germany) holey carbon copper grids, 3 µl of 10-nm colloidal gold in ribosome buffer were added and the sample was vitrified in liquid ethane using a Vitrobot Mark IV (FEI, USA). The Vitrobot was operated at ambient temperature (22 °C) and humidity (60%) using a blotting time of 3 s and a blot force of 0. Tilt series were acquired on an FEI Titan Krios transmission electron microscope equipped with a K2 Summit direct electron detector with a Quantum energy filter (Gatan, USA), operated in movie mode with 4–7 frames per projection image.

Exposure time varied from 0.8 to 1.4 s and 2.0 to 2.8 s for CTM and VPP data acquisition, respectively, due to variations in the FEG output current. Cumulative electron dose was kept constant in all datasets. The TEM was operated at an acceleration voltage of 300 kV, an object pixel size of 2.62 Å, and nominal defocus of 2.4–3.7 µm (defocus dataset) or 0–200 nm (VPP dataset). The standard autofocus procedure implemented in SerialEM was used for focusing. For retention of high-resolution signal in VPP data, it was important to use no defocus offset for focus measurement and to set the target defocus to 0 (Fig. 3). Single-axis tilt series were recorded over an angular range of –60° to +60° in two halves (first half: 20° to –60°; second half: 22° to 60°) with an angular increment of 2° and a cumulative electron dose of 90–100 e[–]/Å² using the SerialEM acquisition software (Mastronarde, 2005). Acquisition of a tomogram took approximately 45 min. Conditioning of the VPP was achieved by pre-irradiation for 60 s after setting the on-plane condition and aligning the beam shift pivot points. The conditioning applied a total dose of 12 nC (0.2 nA beam current * 60 s) to the phase plate which was estimated to generate an initial phase shift of 0.35 π (from Fig. 3 in (Danev and Baumeister, 2016)). Tilt series added a dose of ~30 nC (61 images * 2.5 s exposure * 0.2 nA beam current) which means that at the end of acquiring a tomogram the total dose on the phase plate was ~42 nC corresponding to a phase shift of ~0.55 π. The irradiated area on the VPP was changed after each tomogram.

2.2. Image processing

Frames from the K2 direct electron detector were aligned using in-house developed motion correction software based on the algorithm described in (Li et al., 2013). For the defocus dataset, tilt-dependent, local correction of phase reversals due to the contrast transfer function was performed using MATLAB scripts and PyTom (Hrabe et al., 2012) on single projections, as described in (Eibauer et al., 2012). For the PP dataset, no CTF correction was performed. Tomogram reconstruction (object pixel size: 2.1 nm) and template matching against a single particle cryo-EM reconstruction of the human 80S ribosome (EMD-5592) (Anger et al., 2013) filtered to 5 nm resolution were accomplished using weighted backprojection in PyTom (Hrabe et al., 2012) as described in (Pfeffer et al., 2012). Candidate particles in each tomogram were selected according to Gaussian distributed constrained correlation coefficients obtained from template matching. For the retained particles, 1 × down sampled subtomograms (80³ voxels, object pixel size: 0.524 nm) were reconstructed individually from the weighted aligned projections using the full tilt range (–60° to +60°). After iterative subtomogram alignment and averaging with PyTom (Hrabe et al., 2012), unbinned subtomograms (160³ voxels, object pixel: 0.262 nm) were reconstructed using a reduced tilt range (–20° to +20°) in order to restrict the cumulative electron dose to 30 e[–]/Å². Subtomograms were iteratively aligned with PyTom until convergence, using a single particle reconstruction of the human ribosome (EMD-5592) (Anger et al., 2013) filtered to 2 nm resolution as a reference for the first iteration. For the subsequent iterations, the average from the previous iteration served as a reference. Angular sampling and bandpass filter for alignment were automatically set in PyTom according to the determined resolution from the previous iteration. For analysis of the relationship between particle number and resolution, differently sized subsets of random subtomograms were either averaged using alignment shifts and rotations determined during alignment of the complete set of 1400 subtomograms, or aligned separately only among the reduced number of particles. The resolution of all subtomogram averages was assessed by Fourier shell correlation (FSC = 0.33) against EMD-5592 (Fourier shell cross resolution, FSCR). For visualization, the resolution-limited maps were sharpened using an empirically

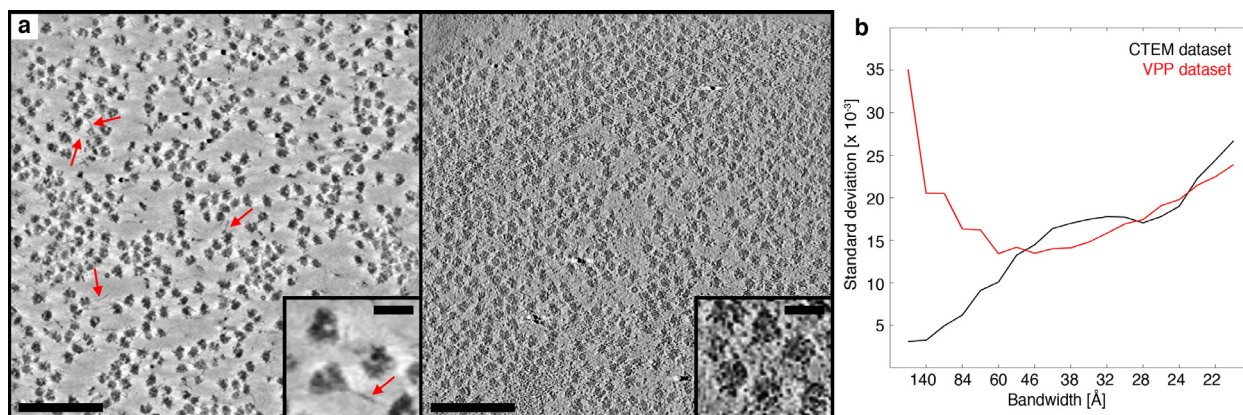


Fig. 1. Ribosomes have more contrast in VPP tomograms. **a**, Slices through unfiltered tomograms (2.1 nm voxel size) acquired either with the VPP at a nominal defocus of 0 nm (left) or CTEM at a nominal defocus of 3.5 μm (right). The inserts show magnified regions of the respective tomogram. Red arrows point at putative ribosomal RNA expansion segments. Scale bars in the full tomogram and the magnified region correspond to 200 nm and 30 nm, respectively. **b**, Mean standard deviation of 100 ribosome-containing subtomograms (1.05 nm voxel size) from the tomograms shown in (a), computed for the given spatial frequencies.

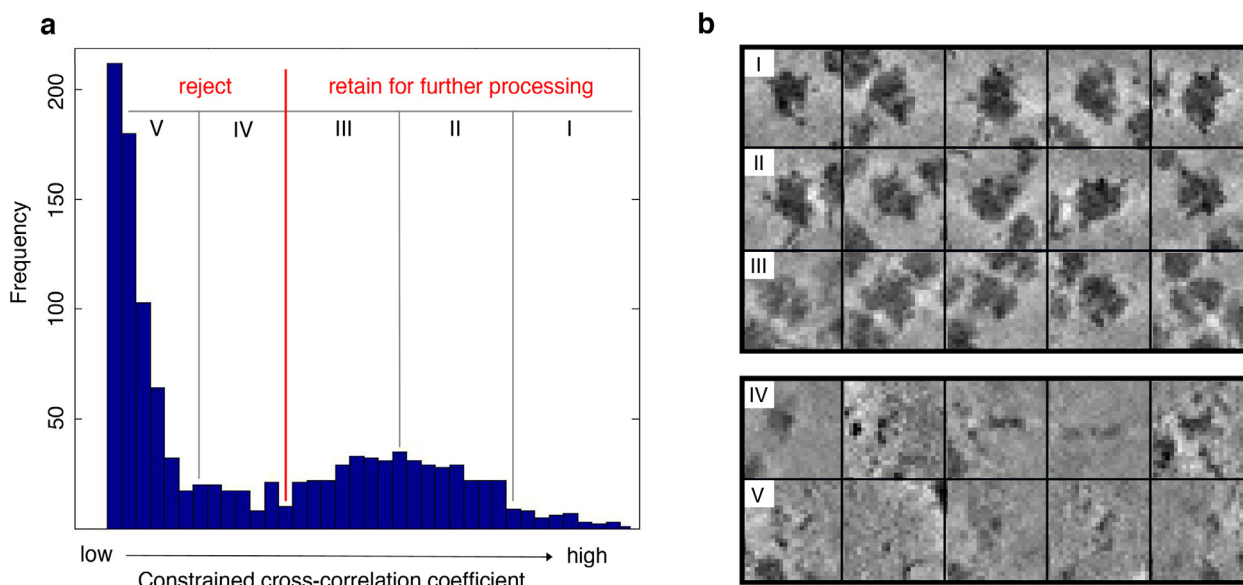


Fig. 2. Particle selection by a cross-correlation based cutoff approach. **a**, Distribution of constrained cross-correlation coefficients retrieved from template matching for a representative tomogram. The correlation cutoff used for particle selection is indicated by a red line. **b**, The range of cross-correlation coefficients was divided into five sections (I–V), as indicated in (a), and central slices of randomly selected subtomograms for each section are shown. The majority of the peaks in sections I–III correspond to 80S ribosomes, while peaks in sections IV–V are mainly false positives.

determined B-factor of -500 . To measure the contrast in data acquired either with the VPP or CTEM, 100 ribosome-containing subtomograms (40^3 voxels, object pixel: 1.048 nm) were extracted directly from tomograms with the corresponding voxel size and their mean standard deviation was computed for all available spatial frequencies.

2.3. Accession codes

The subtomogram averages obtained with CTEM at one defocus value, with CTEM at a range of defocus values and with the VPP have been deposited in the EMDDataBank with accession codes EMD-3419, EMD-3420 and EMD-3418, respectively.

3. Results

3.1. Tomograms acquired with the VPP have higher contrast

Mammalian 80S ribosomes isolated from rabbit reticulocyte lysate were vitrified and tilt series were acquired with either CTEM

at a nominal target defocus of 3.5 μm (10 tomograms) or the VPP using slightly different focusing strategies (10 tomograms, see below). While the tilt images acquired with the VPP were used directly for tomogram reconstruction by weighted back projection, tilt images acquired with CTEM were first corrected for phase reversals due to the oscillating CTF. To this end, we applied a strip-based phase flipping approach that reverts sign changes of the signal in specific frequency bands, taking into account the defocus gradient in tilted images (Eibauer et al., 2012; Fernandez et al., 2006). The amplitudes remained unmodified. In the unfiltered 3D reconstructions, ribosomes are visible for both acquisition approaches, but they stand out from the background more clearly in tomograms acquired with the VPP (Fig. 1a). Long filamentous structures protruding from ribosomes, likely corresponding to the highly flexible ribosomal RNA expansion segments (Melnikov et al., 2012), can be clearly discerned in the VPP tomograms (Fig. 1a). As a measure for the contrast of ribosomes in tomograms acquired with either the VPP or CTEM, we computed the mean standard deviation of 100 ribosome-containing subtomograms for different spatial frequencies. The mean standard deviation,

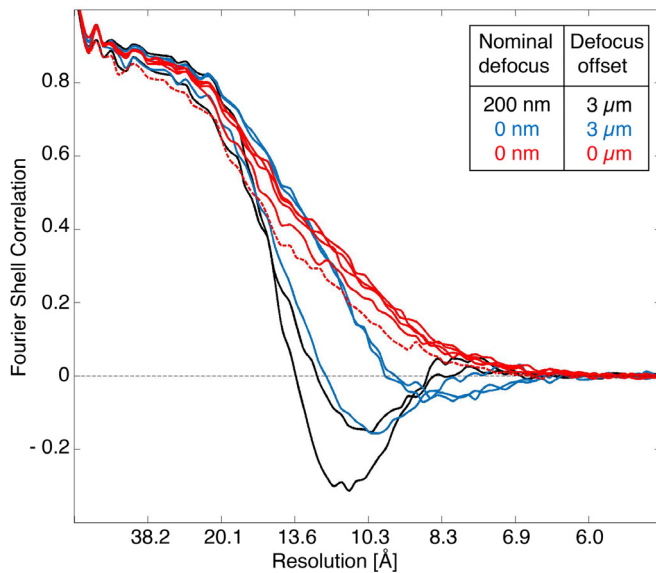


Fig. 3. Evaluation of different focusing strategies for data acquisition with the VPP. Tomograms were acquired with slightly different strategies concerning nominal target defocus and defocus offset for focus measurement (as color-coded in the figure). For each tomogram, approximately 400 aligned subtomograms were averaged and FSCR curves were computed against EMD-5592.

and consequently also the contrast, is significantly (3–10-fold) higher for low-frequency components in subtomograms acquired with the VPP (Fig. 1b).

3.2. Accurate focusing is essential for good VPP performance

Candidate particles were located in the tomograms via a cross correlation-based pattern recognition approach ('template matching') (Frangakis et al., 2002) against a single particle cryo-EM reconstruction of the human 80S ribosome (EMD-5592) (Anger et al., 2013) filtered to 5 nm resolution. Independent of the acquisition approach, the highest-scoring cross-correlation peaks showed a Gaussian distribution, corresponding to true positive matches, followed by a tail of lower scoring cross-correlation peaks from false positive matches (Fig. 2a). By adjusting the position of the cutoff at the lower-end tail of the Gaussian distribution, true positive peaks could be separated efficiently from most false positives, as confirmed by visual inspection of random subtomograms (Fig. 2b). Using this approach, each tomogram yielded 350–450 peaks for further processing. For the retained peaks, subtomograms (80^3 voxels, object pixel: 0.524 nm) were reconstructed individually from the weighted and aligned projections using the full tilt range (-60° to $+60^\circ$). Iterative alignment yielded refined particle coordinates and orientations. Prior to final refinement, the subtomograms were reconstructed from projections covering a reduced tilt range (-20° to 20°) at full spatial sampling using the refined particle coordinates, and iteratively aligned until convergence. Restricting the range of tilt images used for the final reconstruction to only the central 21 projections pursued three specific aims: (i) the cumulative electron dose applied to the sample within these central 21 projections corresponds to only 25–30 $e^-/\text{\AA}^2$ and thus high-resolution information is retained that would otherwise be destroyed by radiation damage. (ii) Due to the applied electron dose, the specimen typically is distorted continuously. This leads to increasingly high alignment residuals for higher tilt angles, which thus should be omitted from the final reconstruction. (iii) Sequential tilting of the specimen results in a predictable defocus gradient perpendicular to the tilt-axis, which

can be compensated by strip-wise CTF correction in CTEM, but not for in-focus data with the VPP, which do show at most one CTF zero. Thus, we limit the negative impact of the defocus gradient on the VPP datasets. The theoretically allowed defocus range as a function of resolution is shown in Supplementary Fig. 1.

For the VPP, data were acquired with strategies that slightly differ for nominal target defocus (0 nm vs. 200 nm) and defocus offset for focus measurement (0 μm vs. 3 μm). Using a beam-tilt focusing scheme, the real defoci used for imaging have a systematic offset of +67.5 nm with respect to the nominal target defoci due to spherical lens aberration (Koster et al., 1987). To compare suitability of the different acquisition strategies for the VPP, we averaged approximately 400 aligned subtomograms for each tomogram separately and computed FSCR curves against the reference structure (EMD-5592). The different acquisition approaches yielded two clearly separable groups of FSCR curves (Fig. 3). Averages from the five tomograms acquired using a combination of 0–200 nm target defocus and 3 μm defocus offset for focus measurement consistently showed negative correlation with the reference structure for parts of the spatial frequency range, suggesting that they were acquired at higher defocus than intended (Fig. 3, black and blue curves). Based on the zero crossings of the FSCR curves, the actual defocus in those tomograms was estimated to be in the range of 250–500 nm, assuming an additional phase shift of 90° for the unscattered electrons. The combination of 0 nm target defocus and no defocus offset for focus measurement yielded by far the best transfer with structural information beyond 1 nm resolution in the averages for five tomograms (Fig. 3, red curves). Since the average from one of the five tomograms acquired using this strategy showed considerably less correlation with the reference, in particular for higher spatial frequencies (Fig. 3, dashed red curve), we omitted that tomogram from further processing and obtained in total 1400 subtomograms from the remaining four VPP tomograms. Judging from the FSCR, averages from all ten tomograms acquired using CTEM were of similar quality (not shown) and 1400 subtomograms from three tomograms were selected for further analysis.

3.3. The VPP out-performs CTEM in subtomogram analysis

According to FSCR against the reference structure (EMD 5592), the resolution of the two subtomogram averages obtained from the remaining ~ 1400 subtomograms acquired either with the VPP or CTEM was estimated to be 9.6 \AA and 10.6 \AA , respectively (Fig. 4a). The FSCR curve of the subtomogram average obtained with CTEM clearly recapitulates oscillations of the CTF (Fig. 4a, black curve): at the CTF zeros crossings the FSCR is markedly reduced, indicating the strongly reduced SNR in the vicinity of these frequencies. In contrast, the FSCR of the subtomogram average obtained with the VPP is not modulated (Fig. 4a, red curve). Visible features, such as the well-resolved ribosomal RNA double helix and rod-shaped densities co-localizing with alpha helices in a superposed atomic model of the ribosome, are consistent with the estimated resolution (Fig. 4c,d and Supplementary Fig. 2a,b).

While normally used in single particle cryo-EM studies, variation of defocus to compensate for frequencies with low signal transfer is not a standard procedure in (cellular) tomography, yet. To address, whether our subtomogram average can be improved using this approach, we acquired another CTEM dataset with slightly varying defocus values in the range of 2.4–3.7 μm . Comparable to the CTEM dataset recorded at a single defocus, averages from all five acquired tomograms were of similar quality and 1400 subtomograms from four tomograms were selected for further analysis ('mixed CTEM dataset'). The FSCR curve of the resulting subtomogram average shows less pronounced oscillations for most of the covered frequency range (Fig. 4b). Only in

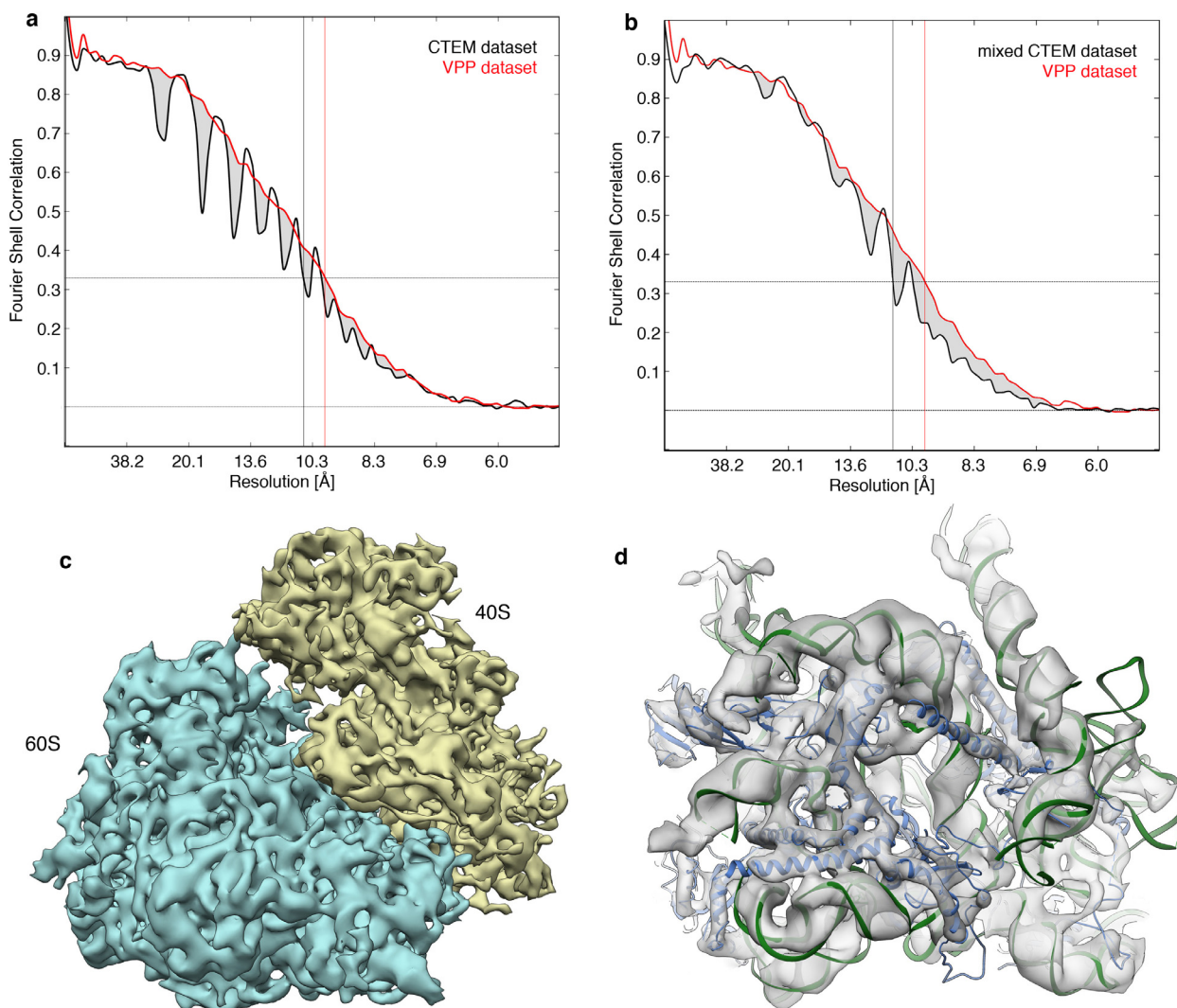


Fig. 4. Structure of the 80S ribosome obtained by subtomogram averaging with the VPP. **a, b** FSC curves against EMD-5592 for subtomogram averages, obtained either using the VPP (red) and CTEM with a single defocus value (**a**, black) or mixed defocus values (**b**, black). Gray areas indicate spatial frequencies with lower signal transfer in CTEM approaches due to CTF oscillations. The resolution of the subtomogram averages was determined to 9.6 Å (VPP), 10.6 Å (CTEM) and 11.2 Å (mixed CTEM), respectively. **c**, Subtomogram average of the 80S ribosome obtained with the VPP filtered to 9.6 Å resolution. The large (60S) and small (40S) ribosomal subunits are depicted in blue and yellow, respectively. **d**, Structural details of the subtomogram average (transparent gray) with atomic models of the ribosomal RNA (green) and ribosomal proteins (blue) superposed.

the resolution range of 10–12 Å, the mixed defocus (2.4, 3.0, 3.3 and 3.7 μm) CTFs seem to coincide, resulting in oscillations of the FSC curve, and thus yielding a resolution of 11.2 Å (Fig. 4b and Supplementary Fig. 2c,d).

To investigate the relation between particle number and resolution of the resulting subtomogram averages for VPP and CTEM acquisition approaches, differently sized subsets of aligned subtomograms were averaged. For each subtomogram average the resolution was determined by FSC (Supplementary Fig. 3) and plotted against the number of subtomograms averaged (Fig. 5a). For a given number of subtomograms, the resolution determined for the VPP dataset is significantly higher than for the CTEM acquisition approaches. In particular, in cellular tomography, where often only one defocus is used for imaging and the number of particles is restricted to several hundred copies, the VPP seems to be highly beneficial in terms of achievable resolution. The FSC curves for the CTEM acquisition approaches (Supplementary Fig. 3b,c) partially recapitulate the oscillations of the CTF, leading to an abrupt increase in resolution once the respective maximum in the FSC curve crosses the resolution criterion. This behaviour is less pronounced in the mixed CTEM dataset, for which signal transfer

is more continuous due to variation of defocus. As a more consistent indicator of signal content, we plotted the area under the FSC curves against the number of particles averaged (Fig. 5b, solid lines). Again, for a given number of subtomograms, the area under the FSC curves and thus the signal content of the averages is higher by ~7% for the VPP dataset than for the CTEM acquisition approaches, mostly due to the lower signal transfer for certain spatial frequencies resulting from oscillations of the CTF (Fig. 4a, b). The signal content for both CTEM acquisition approaches is comparable. Consistent with the higher signal content for averages obtained with the VPP, also individual aligned subtomograms from the VPP dataset show a significantly higher area under the FSC curves when correlated to a missing wedge modified reference structure (Supplementary Fig. 4).

Instead of averaging the subsets of particles using alignment shifts and rotations determined during alignment of the complete set of 1400 subtomograms, we also aligned the subsets of particles separately only within the subsets. As expected, the lower SNR in the iteratively updated reference/average for smaller subsets of particles results in an increased subtomogram alignment error, causing a slight, but systematic decrease of the area under the

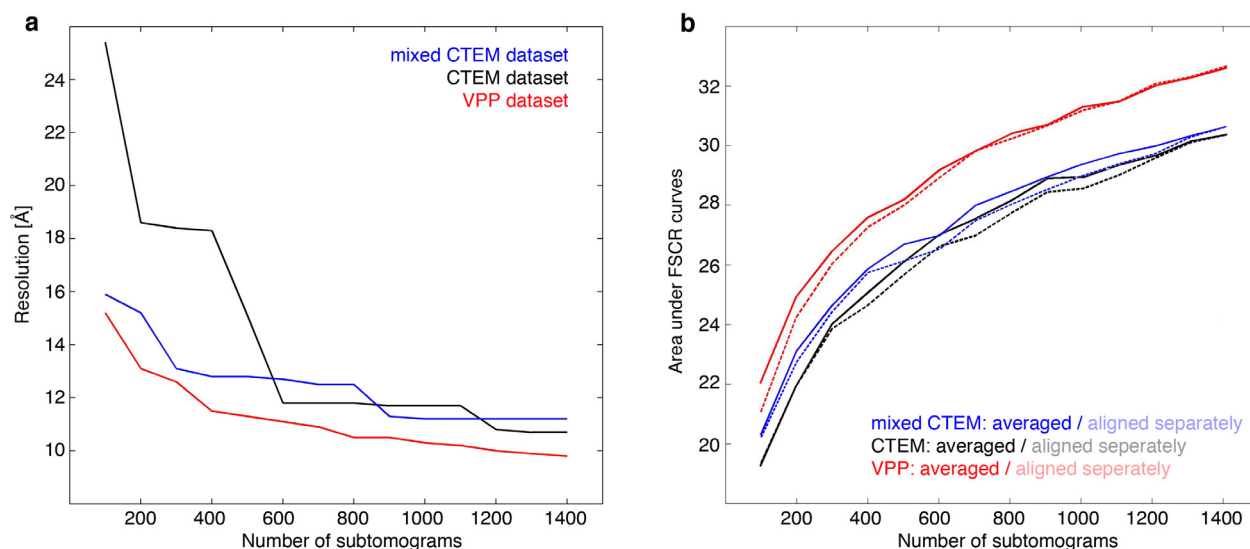


Fig. 5. Relationship between particle number and resolution of subtomogram averages. **a.** Resolution of subset averages plotted against the number of subtomograms used for averaging. Resolution of the averages was determined by FSC against EMD-5592 (Supplementary Fig. 3). **b.** Area under the respective FSC curves (Supplementary Fig. 3), plotted against the number of subtomograms used for averaging. Averages were computed either with shifts and rotations determined during alignment of the complete set of 1400 subtomograms (solid lines), or after aligning the subsets of particles separately only among themselves (dashed lines).

resulting FSC curves (Fig. 5b, dashed lines). This decrease is similar for VPP and CTEM datasets. Furthermore, we tried to estimate the mean alignment error for all subsets of individually aligned subtomograms by comparing their alignment shifts and rotations obtained from alignment either in individual subsets or the full dataset (Supplementary Fig. 5). Consistent with the comparable slight decrease in signal content for subtomogram averages after individual alignment (Fig. 5b), the particle number-dependent alignment error is comparable between all three datasets.

4. Discussion

In this work we assess the performance of the VPP for subtomogram analysis and compare it to CTEM. As expected, due to the continuous signal transfer, starting from low spatial frequencies, the contrast of VPP tomograms is considerably higher than that of CTEM tomograms. Consequently, the raw VPP tomograms show details even on the molecular level, as exemplified by the putative ribosomal RNA expansion segments that can be clearly discerned in those tomograms (Fig. 1). The ability to visualize smaller macromolecular components in single subtomograms will allow for a much more detailed analysis of heterogeneous and pleomorphic specimens that are too flexible to be studied by averaging.

Both VPP and CTEM acquisition approaches yield subtomogram averages at approximately 10–11 Å resolution from only 1400 subtomograms. The FSC curves for the averages obtained with CTEM approaches partially recapitulate CTF oscillations and thus suffer from lower signal transfer for certain spatial frequencies. As expected, oscillations of the FSC curve are less pronounced for the mixed CTEM dataset and a flattening of the curve is achieved. Since the total signal (e.g. the total number of subtomograms) is the same for both CTEM approaches, the less pronounced dips of the FSC curve for the mixed CTEM dataset come at the expense of also less pronounced maxima. In contrast, the FSC curve for the subtomogram average obtained using the VPP shows continuous signal transfer for the whole frequency range. Averaging equally sized subsets of aligned particles yields considerably higher information content for the VPP than for CTEM approaches, as judged by the determined resolutions and the area under the respective FSC curves. This finding is consistent with and likely a main consequence of the lower signal transfer for certain spatial

frequencies upon defocusing necessary for imaging in CTEM. The VPP has some signal loss due to scattering by the phase plate film, as evidenced by the VPP FSC curve being slightly below the maxima of the CTEM curve (Fig. 4a). A “lossless” phase plate should produce a smooth FSC curve enveloping the maxima of the CTEM curve. A rough estimate shows that the area under such an “ideal” phase plate FSC curve will be ~3% larger than that under the VPP curve. This is a relatively small gain compared to the ~7% area increase already provided by the VPP compared to CTEM. Consistent with a mere flattening of the FSC curves for the mixed CTEM dataset, the signal content of the CTEM and mixed CTEM datasets are comparable, as judged by the area under their FSC curves. Aligning the subsets of particles separately only among the reduced number of particles, we observed a minor decrease of the area under the resulting FSC curves for a given subset size. This decrease in area is similar for VPP and CTEM datasets and probably results from the lower SNR in the iteratively updated reference/average for smaller subsets of particles and the resulting higher subtomogram alignment error. We anticipate that the additional low frequency information in subtomograms obtained with the VPP will make a much more significant difference in subtomogram alignment accuracy for smaller complexes with less contrast than the isolated ribosome.

A systematic analysis of different focusing strategies (Fig. 3) underlines the importance of choosing optimal focusing protocols for tomographic data acquisition with the VPP. In this study, the best results were obtained by acquiring data very close to focus with no defocus offset during the focus measurement. In contrast, subtomogram averages from tomograms acquired using a combination of 0–200 nm target defocus and 3 μ m defocus offset for focus measurement consistently showed negative correlation with the reference structure, suggesting the presence of residual defocus (Fig. 3, blue and black curves). The fluctuation of the residual defocus, as well as its deviation from the intended defocus, could be an effect of different inclinations of the grid along the tilt axis, which would lead to a systematic deviation of the measured from the actual defocus values for each tomogram. However, as judged from the orientation of specimen density in the reconstructed 3D volumes, none of the target areas had noteworthy inclination along the tilt-axis. Therefore, we suggest that the observed focusing errors were caused by a combination of the 3 μ m defocus offset

for focus measurement and objective lens hysteresis. Apart from focusing errors, defocus due to sample tilt could also become a limiting factor for close-to-focus work with the VPP. The resolution is limited by the first CTF zero and depending on the tilt angle and the size of the observed area outer parts of the image could become resolution limited. In this work the observed area was $\sim 1 \mu\text{m}$ on edge which means that the outer edges of the image will be limited to 10 \AA resolution (defocus must be $< 200 \text{ nm}$, from [Supplementary Fig. 1](#)) when the sample is tilted above $\sim 24^\circ$. This is one of the reasons, but not the main one, why such tilt angles were not included in the final reconstructions.

A straightforward protocol for accurate focusing with the VPP was recently introduced for single particle cryo-EM ([Danev and Baumeister, 2016](#); [Khoshouei et al., 2016](#)): Focusing is done rigorously (several times for each image) at two positions on opposite sides of the target area. The resulting nominal defocus interpolated from the two focusing areas is a good approximation for the target area. This strategy has proven beneficial for single particle cryo-EM data acquisition with the VPP, where it was key to reach a resolution of 3.2 \AA ([Danev and Baumeister, 2016](#)). However, tilt series acquired using this approach resulted in lower resolutions than the simpler focusing used above (not shown). In the dataset acquired using focus determination on multiple sites the tilt image alignment residuals were very high already at low tilt angles. This increased tomographic alignment error likely arises from deformation of the sample due to the radiation damage at the focusing areas after multiple rounds of focusing. Thus, the beam-induced deformation of the sample due to the lengthy focusing protocol outweighs the benefit of more accurate focusing.

Very much in contrast to the necessity of accurate focusing in VPP imaging, CTEM is largely immune to focusing errors because the defocus is measured and the CTF is corrected on the tilt images themselves. An alternative “hybrid” approach with the VPP would be to apply intentional defocus instead of trying to collect the data perfectly in focus. The CTF could then be fitted and corrected in a similar fashion as with CTEM. In practice, the imaging model would need to be extended by a VPP-induced phase shift in CTF determination and correction. The role of the VPP in such an approach would be restricted to improving the contrast by providing increased transfer for low spatial frequencies. The remaining frequency spectrum, however, will have CTF zeroes and the associated information loss like in CTEM. Practice and further experience with the VPP will show which approach will be most successful for which application. We anticipate that the most appropriate strategy may differ depending on the sample (flatness, stability etc.) and the intended purpose (direct structural interpretation, subtomogram averaging etc.).

Our study highlights that tomographic data acquisition using the VPP requires a lot of care and accuracy in focusing for retaining high-resolution information. However, the effort pays off, because signal is transferred continuously over the whole frequency range, contrast is considerably improved compared to CTEM, and significantly less subtomograms are necessary to obtain averages with a comparable resolution.

Acknowledgment

This work was supported by a grant of the German Research Council (DFG 716/4-1) to F.F.

Appendix A. Supplementary data

Supplementary data associated with this article can be found, in the online version, at <http://dx.doi.org/10.1016/j.jsb.2016.05.009>.

References

- Anger, A.M., Armache, J.P., Berninghausen, O., Habeck, M., Subklewe, M., Wilson, D., Beckmann, R., 2013. Structures of the human and *Drosophila* 80S ribosome. *Nature* 497, 80–85.
- Asano, S., Fukuda, Y., Beck, F., Aufderheide, A., Forster, F., Danev, R., Baumeister, W., 2015. Proteasomes. A molecular census of 26S proteasomes in intact neurons. *Science* 347, 439–442.
- Behrmann, E., Loerke, J., Budkevich, T.V., Yamamoto, K., Schmidt, A., Penczek, P.A., Vos, M.R., Burger, J., Mielke, T., Scheerer, P., Spahn, C.M., 2015. Structural snapshots of actively translating human ribosomes. *Cell* 161, 845–857.
- Ben-Shem, A., Jenner, L., Yusupova, G., Yusupov, M., 2010. Crystal structure of the eukaryotic ribosome. *Science* 330, 1203–1209.
- Ben-Shem, A., Garreau de Loubresse, N., Melnikov, S., Jenner, L., Yusupova, G., Yusupov, M., 2011. The structure of the eukaryotic ribosome at 3.0 \AA resolution. *Science* 334, 1524–1529.
- Brandt, F., Etchells, S.A., Ortiz, J.O., Elcock, A.H., Hartl, F.U., Baumeister, W., 2009. The native 3D organization of bacterial polysomes. *Cell* 136, 261–271.
- Briggs, J.A., 2013. Structural biology in situ—the potential of subtomogram averaging. *Curr. Opin. Struct. Biol.* 23, 261–267.
- Danev, R., Baumeister, W., 2016. Cryo-EM single particle analysis with the Volta phase plate. *Elife*, 5.
- Danev, R., Buijsse, B., Khoshouei, M., Plitzko, J.M., Baumeister, W., 2014. Volta potential phase plate for in-focus phase contrast transmission electron microscopy. *Proc. Natl. Acad. Sci. U.S.A.* 111, 15635–15640.
- Eibauer, M., Hoffmann, C., Plitzko, J.M., Baumeister, W., Nickell, S., Engelhardt, H., 2012. Unraveling the structure of membrane proteins in situ by transfer function corrected cryo-electron tomography. *J. Struct. Biol.* 180, 488–496.
- Fernandez, J.J., Li, S., Crowther, R.A., 2006. CTF determination and correction in electron cryotomography. *Ultramicroscopy* 106, 587–596.
- Forster, F., Hegerl, R., 2007. Structure determination in situ by averaging of tomograms. *Methods Cell Biol.* 79, 741–767.
- Forster, F., Han, B.G., Beck, M., 2010. Visual proteomics. *Methods Enzymol.* 483, 215–243.
- Frangakis, A.S., Bohm, J., Forster, F., Nickell, S., Nicastro, D., Typke, D., Hegerl, R., Baumeister, W., 2002. Identification of macromolecular complexes in cryoelectron tomograms of phantom cells. *Proc. Natl. Acad. Sci. U.S.A.* 99, 14153–14158.
- Fukuda, Y., Laugks, U., Lucic, V., Baumeister, W., Danev, R., 2015. Electron cryotomography of vitrified cells with a Volta phase plate. *J. Struct. Biol.* 190, 143–154.
- Hrabe, T., Chen, Y., Pfeffer, S., Cuellar, L.K., Mangold, A.V., Forster, F., 2012. PyTom: a python-based toolbox for localization of macromolecules in cryo-electron tomograms and subtomogram analysis. *J. Struct. Biol.* 178, 177–188.
- Jenner, L., Melnikov, S., Garreau de Loubresse, N., Ben-Shem, A., Iskakova, M., Urzhumtsev, A., Meskauskas, A., Dinman, J., Yusupova, G., Yusupov, M., 2012. Crystal structure of the 80S yeast ribosome. *Curr. Opin. Struct. Biol.* 22, 759–767.
- Khoshouei, M., Radjainia, M., Phillips, A.J., Gerrard, J.A., Mitra, A.K., Plitzko, J.M., Baumeister, W., Danev, R., 2016. Volta phase plate cryo-EM of the small protein complex Prx3. *Nat. Commun.* 7, 10534.
- Koster, A.J., Van den Bos, A., Van der Mast, K.D., 1987. An autofocus method for a TEM. *Ultramicroscopy* 21, 209–222.
- Li, X., Mooney, P., Zheng, S., Booth, C.R., Braunfeld, M.B., Gubbens, S., Agard, D.A., Cheng, Y., 2013. Electron counting and beam-induced motion correction enable near-atomic-resolution single-particle cryo-EM. *Nat. Methods* 10, 584–590.
- Lucic, V., Rigort, A., Baumeister, W., 2013. Cryo-electron tomography: the challenge of doing structural biology in situ. *J. Cell Biol.* 202, 407–419.
- Mahamid, J., Pfeffer, S., Schaffer, M., Villa, E., Danev, R., Kuhn-Cuellar, L., Förster, F., Hyman, A., Plitzko, J., Baumeister, W., 2016. Visualizing the molecular sociology at the HeLa cell nuclear periphery. *Science* 351, 969–972.
- Mastrorade, D.N., 2005. Automated electron microscope tomography using robust prediction of specimen movements. *J. Struct. Biol.* 152, 36–51.
- Melnikov, S., Ben-Shem, A., Garreau de Loubresse, N., Jenner, L., Yusupova, G., Yusupov, M., 2012. One core, two shells: bacterial and eukaryotic ribosomes. *Nat. Struct. Mol. Biol.* 19, 560–567.
- Myasnikov, A.G., Afonina, Z.A., Menetret, J.F., Shirokov, V.A., Spirin, A.S., Klaholz, B.P., 2014. The molecular structure of the left-handed supra-molecular helix of eukaryotic polyribosomes. *Nat. Commun.* 5, 5294.
- Pfeffer, S., Brandt, F., Hrabe, T., Lang, S., Eibauer, M., Zimmermann, R., Forster, F., 2012. Structure and 3D arrangement of endoplasmic reticulum membrane-associated ribosomes. *Structure* 20, 1508–1518.
- Pfeffer, S., Dudek, J., Gogala, M., Schorr, S., Linxweiler, J., Lang, S., Becker, T., Beckmann, R., Zimmermann, R., Forster, F., 2014. Structure of the mammalian oligosaccharyl-transferase complex in the native ER protein translocon. *Nat. Commun.* 5, 3072.
- Pfeffer, S., Woellhaf, M.W., Herrmann, J.M., Forster, F., 2015. Organization of the mitochondrial translation machinery studied in situ by cryoelectron tomography. *Nat. Commun.* 6, 6019.
- Scheres, S.H., Chen, S., 2012. Prevention of overfitting in cryo-EM structure determination. *Nat. Methods* 9, 853–854.
- Schwurth, B.S., Borovinskaya, M.A., Hau, C.W., Zhang, W., Vila-Sanjurjo, A., Holton, J.M., Cate, J.H., 2005. Structures of the bacterial ribosome at 3.5 \AA resolution. *Science* 310, 827–834.

- Selmer, M., Dunham, C.M., Murphy, F.V.T., Weixlbaumer, A., Petry, S., Kelley, A.C., Weir, J.R., Ramakrishnan, V., 2006. Structure of the 70S ribosome complexed with mRNA and tRNA. *Science* 313, 1935–1942.
- Steitz, T.A., 2008. A structural understanding of the dynamic ribosome machine. *Nat. Rev. Mol. Cell Biol.* 9, 242–253.
- Voorhees, R.M., Fernandez, I.S., Scheres, S.H., Hegde, R.S., 2014. Structure of the mammalian ribosome-Sec61 complex to 3.4 Å resolution. *Cell* 157, 1632–1643.
- Yusupov, M.M., Yusupova, G.Z., Baucom, A., Lieberman, K., Earnest, T.N., Cate, J.H., Noller, H.F., 2001. Crystal structure of the ribosome at 5.5 Å resolution. *Science* 292, 883–896.